BULLETIN OF THE POLISH ACADEMY OF SCIENCES
TECHNICAL SCIENCES, Vol. 73(4), 2025, Article number: e154271
DOI: 10.24425/bpasts.2025.154271

Strain-controlled uniaxial fatigue of an AA2519 aluminium alloy sheet

Łukasz PEJKOWSKI and Maciej KOTYK*

Faculty of Mechanical Engineering, Bydgoszcz University of Science and Technology, Kaliskiego 7, 85-796 Bydgoszcz, Poland

Abstract. This study provides a comprehensive investigation of the uniaxial, strain-controlled fatigue behaviour of an AA2519 aluminium-copper alloy. The alloy was characterized in the as-fabricated state. Three orientations relative to the rolling direction were used to determine the mechanical properties. The quasi-static strength and cyclic stress-strain response of the AA2519 aluminium alloy for the examined cases were similar regardless of the rolling direction, although slight differences between them were noticeable. Similarly, the fatigue life was not strongly affected by the specimen orientation. The investigation also included fractographic analysis of the fracture surfaces, revealing differences between strain amplitude levels and specimen orientations. The experimental results obtained provide a good basis for engineering applications of the analyzed AA2519 alloy and offer a solid foundation for further research into the effect of heat treatment on the fatigue strength of the investigated alloy.

Keywords: AA2519; aluminium alloy; sheet metal; fatigue life.

1. INTRODUCTION

Engineering structures, despite their wide diversity, primarily because of their intended purpose, share a common characteristic, i.e., during the design process, efforts are made to ensure that the developed structure exhibits the smallest possible mass while retaining its mechanical properties, such as stiffness and load-carrying capacity. In certain applications, such as aerospace, this issue holds particular significance, primarily because of energy consumption, as lighter aircraft consume less fuel, leading to an increased range per refuelling. The benefit derived from reduced mass extends to almost all industrial sectors.

A significant breakthrough in the selection of engineering materials, considering a more favourable density-to-strength ratio than steel, was the development of the first duralumin by Alfred Wilhelmy [1]. This discovery subsequently contributed to the emergence of advanced, lightweight aerospace and space structures [2–5], including those with military applications [6]. The AA2519 alloy is an interesting material within this group because of its technological and mechanical properties, such as high strength, ballistic resistance, and stress corrosion resistance [7–11]. These mechanical properties, along with the development of welding technology for sheets made from this alloy, make it a material that can be successfully used in lightweight armoured vehicles and aviation. Because of its significantly lower mass compared to steel, the possibility of using this alloy for aircraft armour has been considered [12]. With the development of explosive welding technology for joining materials with different properties [13], the AA2519 alloy found its application in the production of Al-Ti layered plates [3, 14–17], which combines the desired mechanical and physicochemical properties.

To enable the commercial application of specified composite, it is necessary to identify its mechanical properties, including a description of the same mechanical characteristics of its base materials. However, in the case of AA2519 aluminium alloy, some of these properties are not available in publicly accessible literature.

AA2519 alloy, similar to other materials in the 2XXX group [18, 19], undergoes changes in its mechanical properties after heat treatment, as well as other aluminium alloys that are strengthened by precipitation [20, 21]. Therefore, several published studies investigated the influence of such treatment on selected mechanical properties and the microstructure of the analyzed material [22–24]. Most of these studies focused on tensile properties, hardness, changes in microstructure [25, 26] and high cycle fatigue live [27]. Other papers provide information on the impact of alloying additives on the mechanical properties [28], including the tensile strength [29–32]. The fracture toughness of the AA2519 alloy was also investigated [33, 34].

As mentioned earlier despite its interesting properties, the fatigue endurance of AA2519 alloys has not been extensively described in the literature. Research on the fatigue durability of the material was presented in [35]. However, the study had a comparative nature, and fatigue test results were presented for various aluminium alloys in the 2XXX series but for a single level of loading. As a result, a fatigue curve was not constructed. As in the previous case, fatigue tests were conducted on heat-treated material (T62) with a strain ratio of $R_\varepsilon = 0.1$. An attempt was made to determine the fatigue durability of the de-

*e-mail: mackot001@pbs.edu.pl

Manuscript submitted 2024-11-08, revised 2025-01-29, initially accepted for publication 2025-03-17, published in July 2025.

scribed AA2519-T62 alloy using specimens taken from extruded profiles. In [36], the Basquin–Manson–Coffin and Ramberg–Osgood curves were obtained for specimens obtained from the profiles; however, for $R_\varepsilon = 0.1$. Another publication by Kosturek *et al.* regarding the durability of AA2519 is [37], where the influence of tool rotational speed during friction stir welding on joint durability between two parts of the AA2519 alloy was investigated. The determination of the mechanical properties involved tensile strength and low-cycle fatigue testing at $R_\varepsilon = 0.1$.

The AA2519 alloy is mainly available as rolled sheet metal. An essential element of such a production process is significant initial plastic deformation and the emergence of directional structure in the material [38,39]. Based on the literature analysis, it was not possible to find complementary information on the fatigue behaviour of AA2519 aluminum alloy sheets considering the rolling direction effect. Therefore, the present study aimed to determine the cyclic stress-strain response and fatigue life of AA2519 specimens cut in three different orientations regarding the rolling direction. The research also includes the analysis of fracture surfaces.

2. MATERIALS AND METHODS

The material used in the study was an AA2519 aluminium alloy rolled sheet in the as-fabricated condition. Table 1 provides the chemical composition of the material. The microstructure of the rolled sheet is shown in Fig. 1. The metallographic sample was polished with a final pass through a 1 μm diamond suspension. Etching was performed using Keller's reagent (95 ml H_2O + 2.5 ml HNO_3 + 1.5 ml HCl + 1 ml HF) for 20 s, then using Weck's reagent (100 ml H_2O + 4 g $KMnO_4$ + 1 g NaOH) for 40 s, and then again using Keller's reagent for 10 s. Figure 1a shows the microstructure perpendicular to the rolling direction. The etching did not reveal the grain structure; however, some basic features can be seen. Precipitates can be seen as brighter areas surrounded by more etched, dark areas. Figure 1b shows the microstructure in the rolling direction. A band structure typical for rolled sheets [40–42] and extruded billets [43] was revealed.

Table 1
Chemical composition of AA2519 alloy

Si	Fe	Cu	Mg	Zn	Ti	V	Zr	Al
0.06	0.08	5.77	0.18	0.01	0.04	0.12	0.2	balance

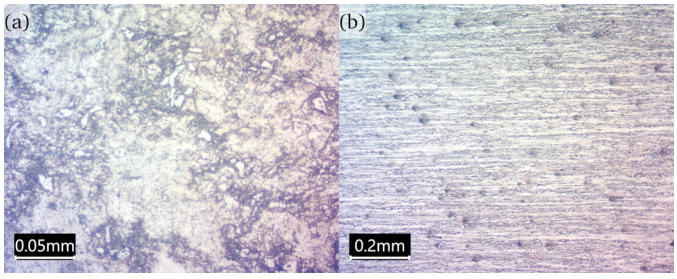

Fig. 1. Microstructure of the rolled AA2519 aluminium alloy sheet: (a) transverse direction and (b) rolling direction

The specimens of dimensions given in Fig. 2 were cut from a 10 mm thick sheet using the wire cutting method (Fig. 3a), ensuring an uninterrupted and stable process of specimen production. To consider the effect of rolling and possible anisotropic properties of the sheet, three groups of specimens were prepared, as shown in Fig. 3c. They were cut along the rolling direction (0°), at 45° to the rolling direction, and transversely (90°).

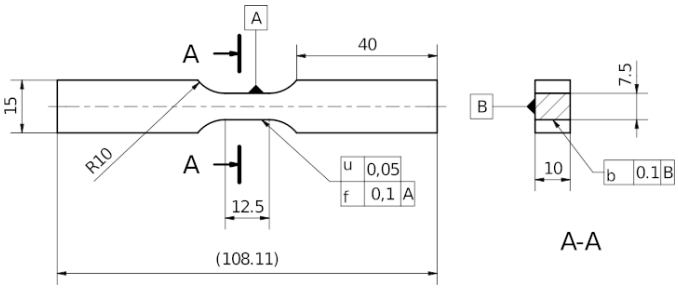

Fig. 2. Dimensions of the specimens used in the study

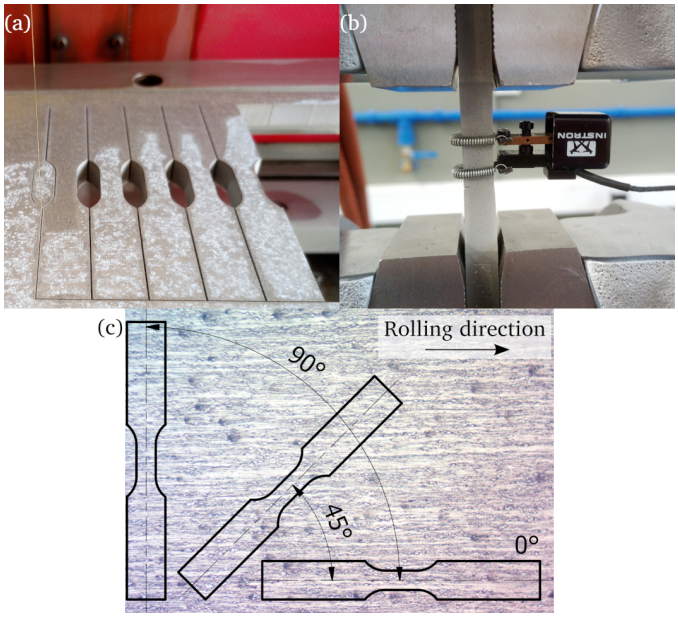

Fig. 3. (a) Specimen preparation, (b) testing setup, and (c) specimen orientation

3. RESULTS AND DISCUSSION

3.1. Monotonic tension tests

The monotonic engineering stress-strain curves are presented in Fig. 4, and the determined basic mechanical properties are compiled in Table 2. The monotonic behaviour of specimens cut at different orientations was not significantly different. As shown in Table 2, the values of the obtained parameters are not different. The differences in the parameters for 0° and the

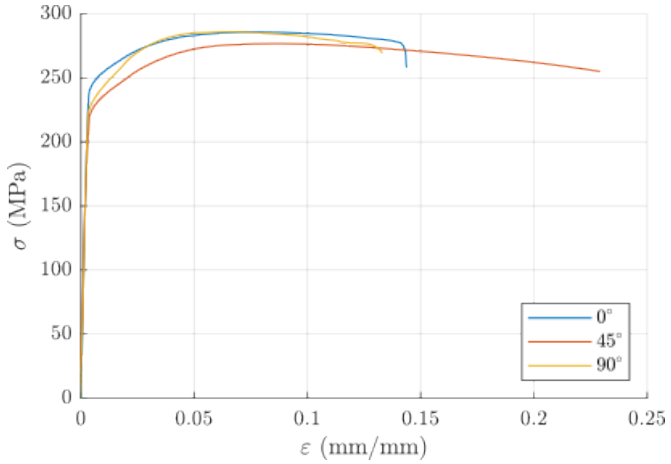

Fig. 4. Monotonic stress-strain curves obtained from uniaxial tensile testing of the AA2519 alloy

Table 2
The basic mechanical properties of the AA2519 alloy were determined via tensile tests

		Young's modulus E		Ultimate tensile strength R_m		Offset yield stress $R_{p0.2}$	
		GPa	% of 0°	MPa	% of 0°	MPa	% of 0°
Orientation	0°	71.8	–	285.8	–	245	–
	45°	67.6	94.2	277.0	96.9	227	92.7
	90°	73.4	102.2	286.6	100.3	234	95.5

other two directions are less than 10%. However, if details are to be sought, one can observe that the curve for the 45° direction is placed below the two others, and the strain at failure was higher by approximately 60%. The offset yield stress values are arranged in the order of 45° < 90° < 0°. Similarly, a low effect of specimen cutting direction on the rolling direction of tensile properties was also reported for other aluminium alloys [44–49].

3.2. Cyclic stress-strain behaviour

Figure 5 presents the strain hysteresis loops determined in the midlife for each specimen cutting direction. The lowest levels of loading were excluded from the charts, as the response was purely or nearly purely elastic. The loops were shifted so that their points of loading inversion were in the common origin 0 [50]. In the case of the 0° orientation (Fig. 5a), the upper branches of the loops form an approximately common curve, although they do not match perfectly. For the two other orientations (Fig. 5b, 5c), the hysteresis loops obtained at lower strain amplitudes stand out from the rest. The main reason is the different slopes of the elastic parts. It can be concluded that the stiffness of the material decreased when subjected to high strain amplitudes. The upper branches of the high-strain hysteresis loops roughly form a common curve, as with the 0° specimen orientation. Figure 5d compares the strain hysteresis loops obtained at strain amplitudes of 0.010, 0.006, and 0.004. Except for the highest loading, for which the stress ranges are equal, they are arranged in ascending order of 45° < 0° < 90°, considering the specimen cut direction.

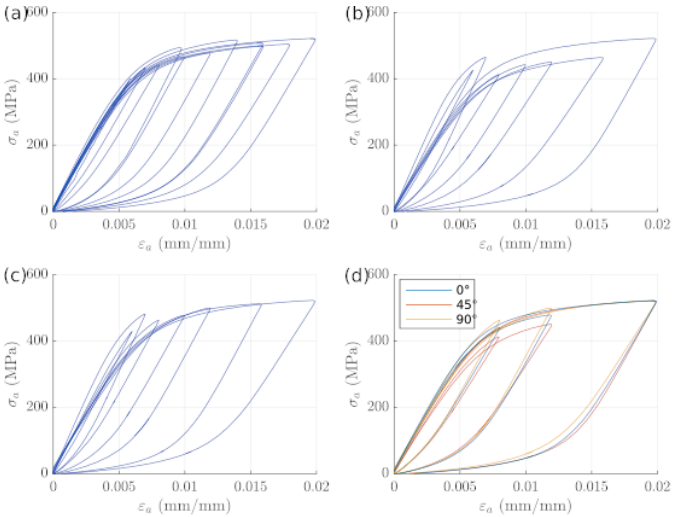

Fig. 5. Midlife strain hysteresis loops for specimens cut at (a) 0°, (b) 45°, and (c) 90° to the rolling direction and (d) comparison

Based on the strain and stress amplitudes, the Ramberg–Osgood curves were fitted to approximate the cyclic stress-strain behaviour of each specimen group [51]:

$$\varepsilon_a = \varepsilon_a^e + \varepsilon_a^p = \frac{\sigma_a}{E} + \left(\frac{\sigma_a}{K'}\right)^{1/n'}, \tag{1}$$

where ε_a is the total strain amplitude, ε_a^e is the elastic strain amplitude, ε_a^p is the plastic strain amplitude, K' is the cyclic strength coefficient, and n' is the cyclic strain hardening exponent. The determined parameters are listed in Table 3. Nonlinear least-square fitting based on the trust region algorithm was used to determine the curves (Fig. 6). A fragment of the monotonic stress-strain curve was additionally imposed to compare monotonic and cyclic stress-strain behaviour [52]. For the 0° and 45° cutting directions (Fig. 6a, 6b), the cyclic yield stress was slightly lower than the monotonic yield stress, and the curve trends show very minor cyclic hardening. In the case of the

Table 3
Ramberg–Osgood equation parameters for the AA2519 alloy considering the cut orientation of the specimen with respect to the rolling direction

		Young's modulus E (GPa)	Cyclic strength coefficient K' (MPa)	Cyclic strain hardening exponent n' (–)
Orientation	0°	78.7	430.1	0.099
	45°	79.7	554.1	0.150
	90°	77.0	351.6	0.059
	all	77.0	397.2	0.083

90° cutting direction (Fig. 6c), little cyclic hardening can be observed, and the monotonic and cyclic yield stresses are identical. Because the cyclic stress-strain response of specimens cut in different directions was similar, another curve was fitted to all the collected data points (Fig. 6d). Figure 6e compares the Ramberg–Osgood curves for all three cutting directions determined separately and altogether. The curves are quite similar, and the curves determined for all the data points approximate the overall stress-strain relationship well.

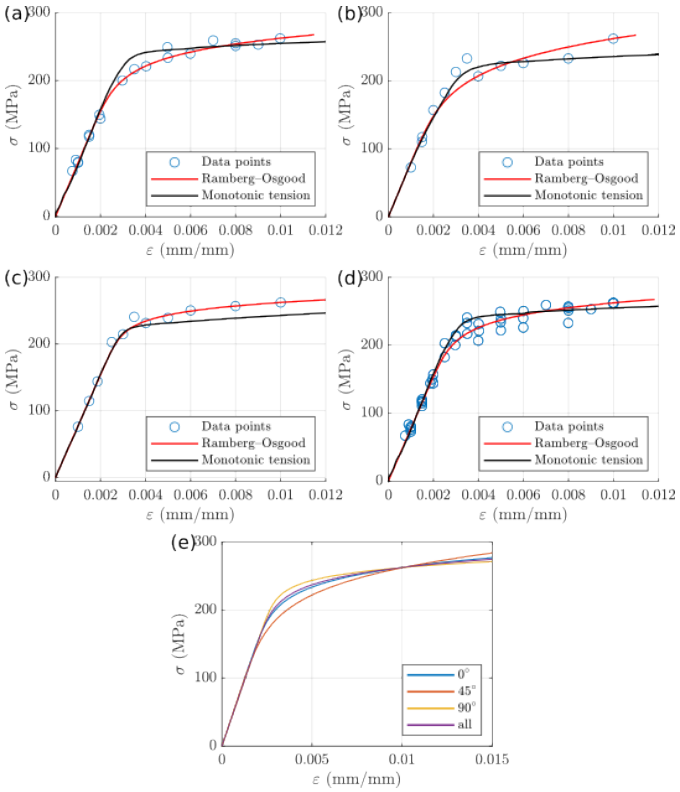

Fig. 6. Ramberg–Osgood curve determination for specimens cut at (a) 0°, (b) 45°, and (c) 90° to the rolling direction, (d) all the directions together, and (e) comparison

The evolution of stress during the tests is shown in Fig. 7 for selected strain amplitude levels. The charts present the amplitudes and means of stress for each cycle. In all three specimen configurations, the results indicate that the stress response remained highly stable during the tests. Based on the observation, the failure criterion was set to a 10% decrease in the axial force compared to the midlife value. Furthermore, the stress response was quite symmetrical, as the means of the amplitudes were low. However, the means are not perfectly zero, which is most likely caused by some positive residual stresses being a consequence of the processing history.

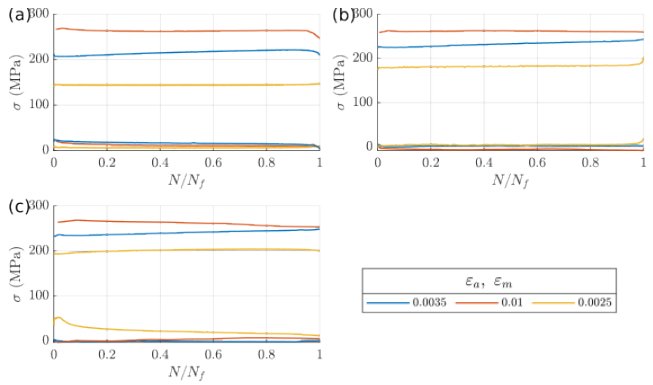

Fig. 7. Stress evolution during the fatigue tests for selected levels of strain amplitude for specimens cut at (a) 0°, (b) 45°, and (c) 90° to the rolling direction

3.3. Fatigue life

The results of uniaxial, fully reversed, strain-controlled fatigue tests are presented in Fig. 8–11 and summarized in Table 4.

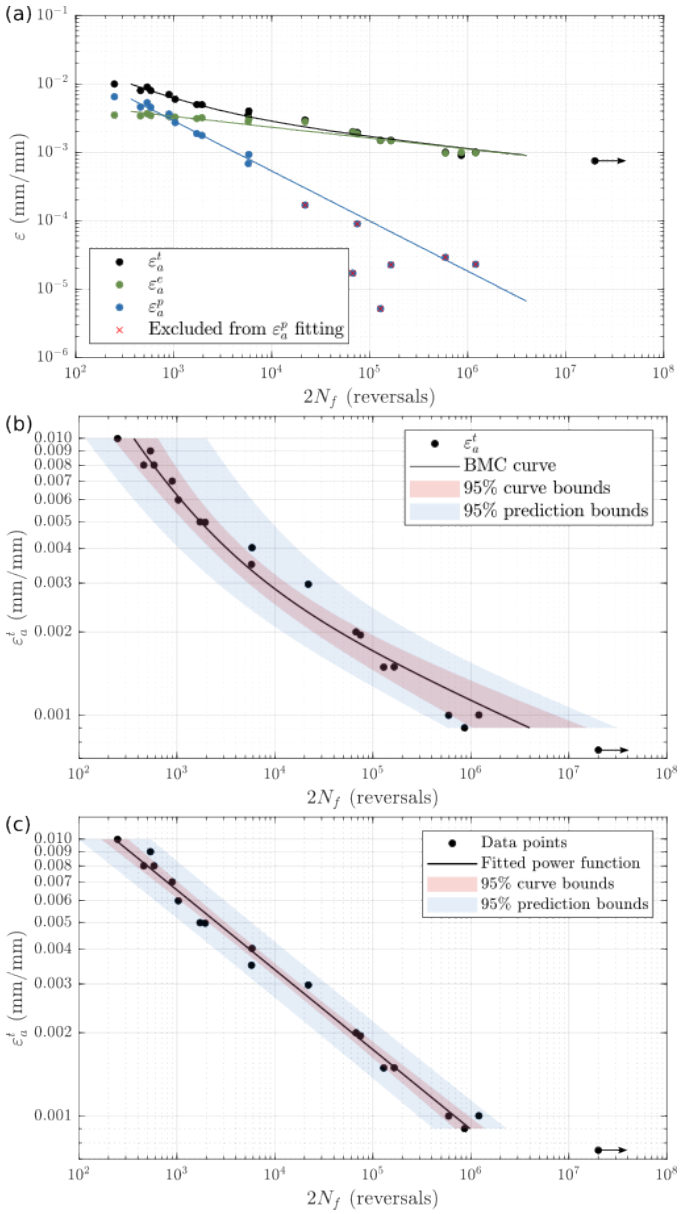

Fig. 8. ε–N curves for 0° specimen cutting direction: (a) Basquin–Manson–Coffin curve and its elastic and plastic components, (b) Basquin–Manson–Coffin alone, (c) power curve

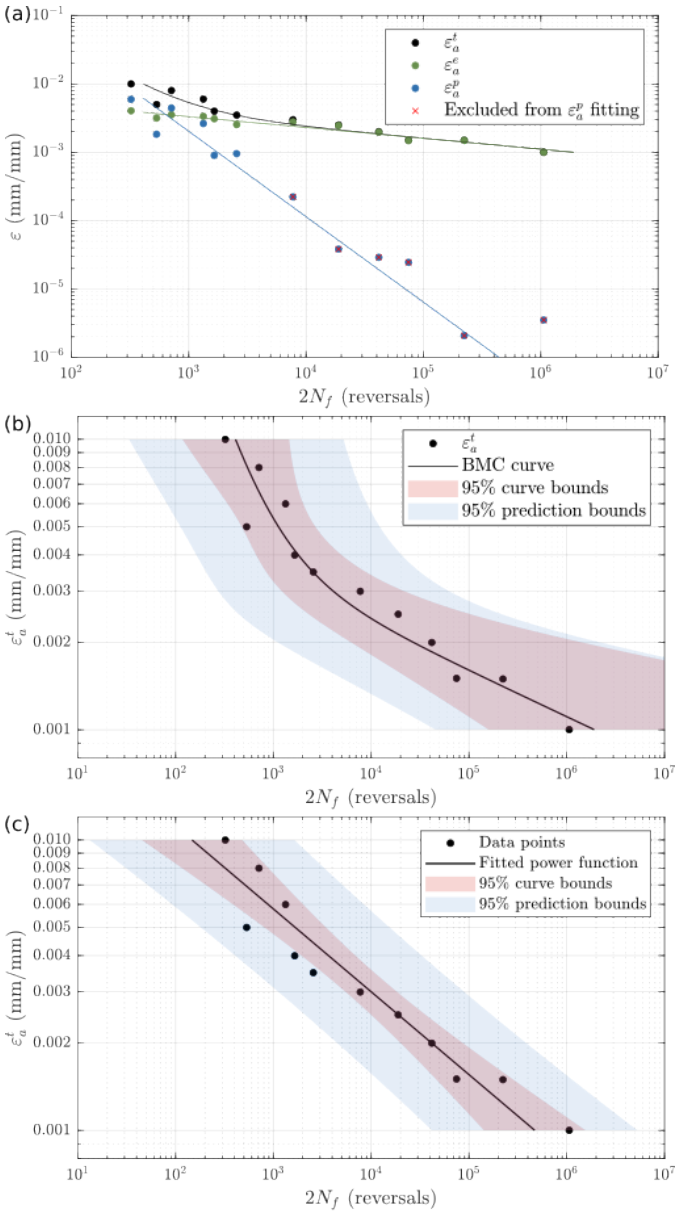

Fig. 9. ε–N curves for 45° specimen cutting direction: (a) Basquin–Manson–Coffin curve and its elastic and plastic components, (b) Basquin–Manson–Coffin alone, (c) power curve

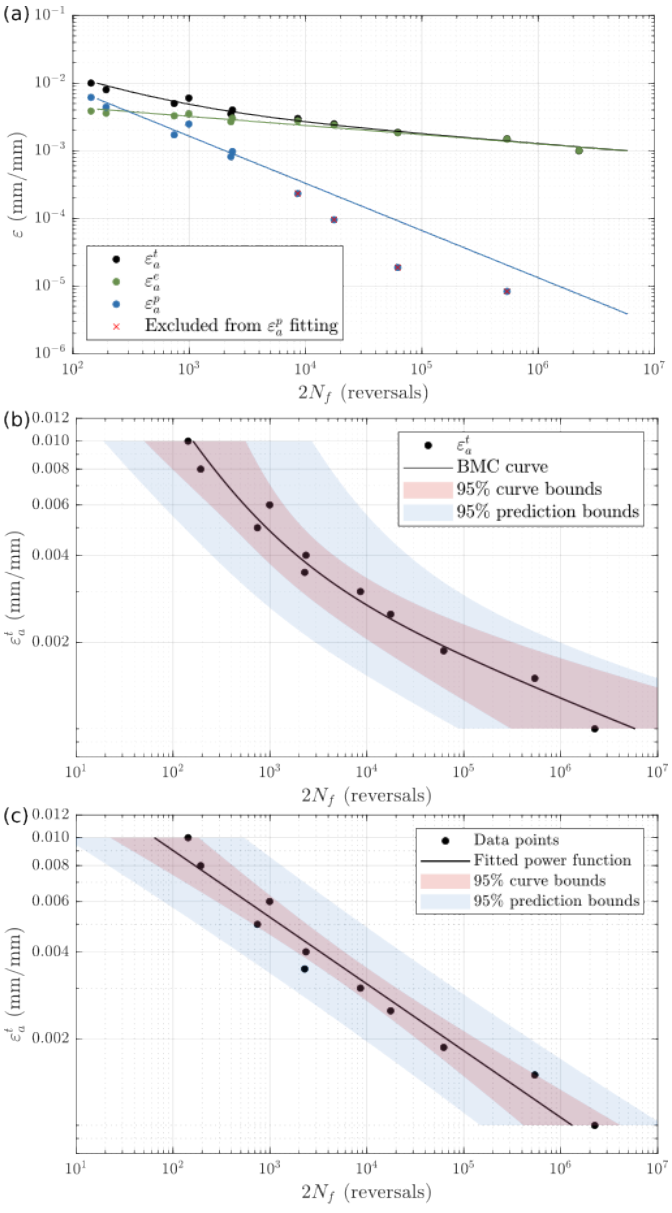

Fig. 10. ε–N curves for 90° specimens cutting direction: (a) Basquin–Manson–Coffin curve and its elastic and plastic components, (b) Basquin–Manson–Coffin alone, (c) power curve

Typical strain-life curves were fitted first using the Basquin–Manson–Coffin (BMC) equation [53]

$$\varepsilon_a = \varepsilon_a^e + \varepsilon_a^p = \frac{\sigma_f'}{E}\left(2N_f\right)^b + \varepsilon_f'\left(2N_f\right)^c, \tag{2}$$

where σ_f' is the fatigue strength coefficient, ε_f' is the fatigue ductility coefficient, b is the fatigue strength exponent, and c is the fatigue ductility exponent. The curves are presented in Fig. 8a, Fig. 9a, and Fig. 10a (black lines), together with the elastic part fitted with the Basquin equation [54] divided by E (green lines) and the plastic part fitted with the Manson–Coffin equation [55, 56] (blue lines). Some data points were excluded from the plastic strain curve fitting. For these points, the plastic strain is calculated as

$$\varepsilon_a^p = \varepsilon_a - \varepsilon_a^e = \frac{\Delta\varepsilon}{2} - \frac{\Delta\sigma}{2E}, \tag{3}$$

and was mostly a result of noise in discrete data, as the stress-strain response was nearly fully elastic. The threshold plastic strain was set to 0.0005, and below this value, the points were rejected from fitting (marked with red crosses). A nonlinear least-square fitting based on the trust region algorithm was used to fit the curves. Figures 8b, 9b, and 10b present the BMC curves with 95% curves and prediction confidence bands. Although the coefficient of determination, R^2, reached very high values (see

Table 4
Results of fatigue tests

0°				45°				90°			
ε_a (mm/mm)	$2N_f$ (reversals)	$\Delta\sigma/2$ (MPa)	E (GPa)	ε_a (mm/mm)	$2N_f$ (reversals)	$\Delta\sigma/2$ (MPa)	E (GPa)	ε_a (mm/mm)	$2N_f$ (reversals)	$\Delta\sigma/2$ (MPa)	E (GPa)
0.0009	862 334	83.3	83.9	0.0010	1 060 544	72.6	72.8	0.0010	2 248 410	76.0	76.0
0.0010	593 403	79.0	81.3	0.0015	222 703	110.3	73.8	0.0015	540 403	114.6	77.0
0.0010	1 207 005	80.1	81.8	0.0015	74 703	117.2	79.3	0.0019	62 103	143.9	78.0
0.0015	129 043	120.1	80.7	0.0020	41 703	156.9	79.7	0.0025	17 603	202.8	84.3
0.0015	165 012	117.4	79.7	0.0025	18 903	182.4	74.1	0.0030	8 583	214.5	77.6
0.0019	74 796	149.6	80.5	0.0030	7 743	212.9	76.7	0.0035	2 283	240.6	89.8
0.0020	67 342	143.9	72.7	0.0035	2 563	232.7	91.7	0.0040	2 353	231.4	76.2
0.0030	21 944	200.1	71.4	0.0040	1 653	206.6	66.8	0.0050	743	239.0	72.8
0.0035	5 775	216.7	76.8	0.0050	533	221.8	70.1	0.0060	993	250.3	71.1
0.0040	5 846	221.0	71.3	0.0060	1 333	226.0	67.2	0.0080	193	256.7	71.7
0.0050	1 946	249.0	77.6	0.0080	713	232.7	65.6	0.0100	143	262.2	67.9
0.0050	1 724	233.6	75.0	0.0100	323	261.8	64.8				
0.0060	1 034	239.6	73.4								
0.0070	896	259.1	76.7								
0.0080	585	250.9	72.7								
0.0080	459	255.0	74.8								
0.0090	537	252.9	68.8								
0.0100	249	262.2	75.0								

Table 5), the BMC curves did not follow the overall trends of the data points perfectly well. Therefore, the data points were also fitted using the power equation, which is identical to Basquin's formula

$$\varepsilon_a = C\left(N_f\right)^a, \tag{4}$$

where C and a are the fitting coefficient and exponent, respectively. All the determined strain-life curves are compared in Fig. 11a and 11b. It can be seen from the comparison that the orientation of the specimens regarding the sheet rolling direction did not result in a significant impact on the fatigue life. Hence, the strain-life curves were also fitted to the data points altogether. As presented in Section 3.2, the stress-strain response was similar for all the specimen groups, and the stress was quite stable during the entire test. Therefore, based on the midlife strain hysteresis loops, an approximated, double-sloped S-N [57] curve was determined (Fig. 11c). All the fitting coefficients are shown in Table 5 and Table 6.

Table 5
Fitting coefficients for the BMC and power strain-life equations

		BMC					Power curve	
		E_m (GPa)	σ'_f (MPa)	b (–)	ε'_f (mm/mm)	c (–)	C (mm/mm)	a (–)
Orientation	0°	$R^2 = 0.93$			$R^2 = 0.97$		$R^2 = 0.99$	
		76.3	773.4	–0.160	0.454	–0.732	0.048	–0.288
	45°	$R^2 = 0.90$			$R^2 = 0.65$		$R^2 = 0.93$	
		73.6	729.8	-0.159	11.41	-1.250	0.041	-0.285
	90°	$R^2 = 0.90$			$R^2 = 0.93$		$R^2 = 0.96$	
		76.6	629.7	-0.135	0.203	-0.698	0.026	-0.232
	all	$R^2 = 0.91$			$R^2 = 0.77$		$R^2 = 0.95$	
		75.6	720.6	-0.153	0.772	-0.848	0.037	-0.267

Table 6
Fitting coefficients for the double-sloped S-N curve

Slope 1		Slope 2	
$R^2 = 0.74$		$R^2 = 0.88$	
σ'_{f1} (MPa)	b_1 (–)	σ'_{f2} (MPa)	b_2 (–)
416.7	–0.079	1689.8	–0.221

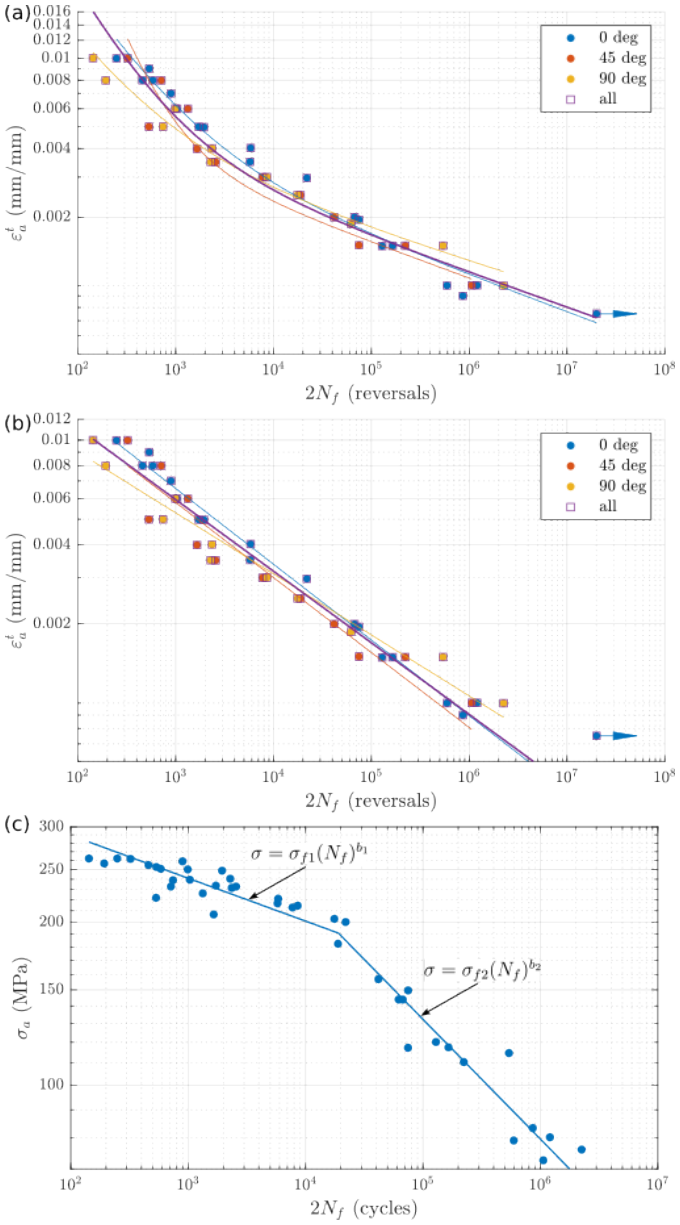

Fig. 11. A comparison of: (a) Basquin–Manson–Coffin, (b) power ε–N, and (c) two-slope Basquin σ–N curves for different specimens cutting orientations

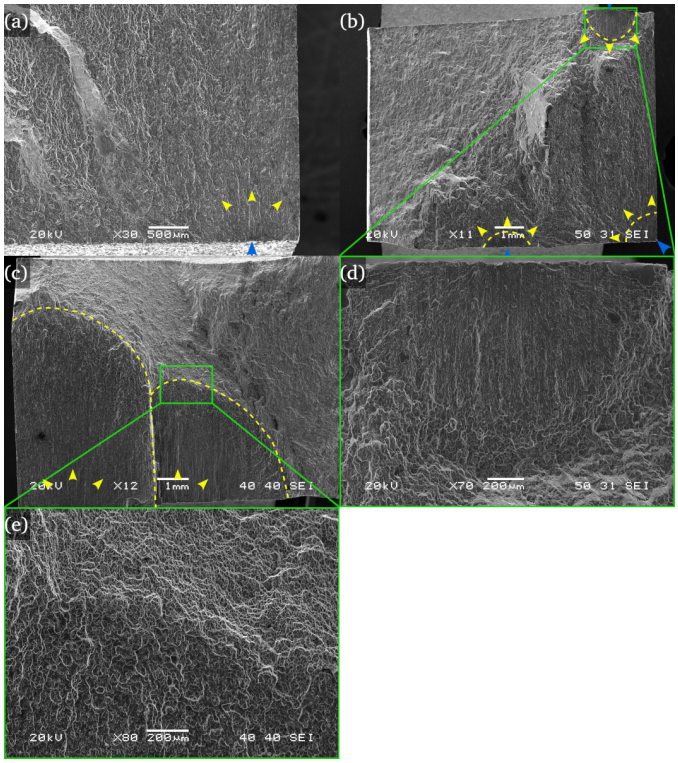

Fig. 12. Fractures of specimens loaded with $\varepsilon_a = 0.001$ mm/mm cut at: (a) 0°, (b) 45°, and (c) 90°, with respect to the rolling direction; (d) and (e) – magnifications

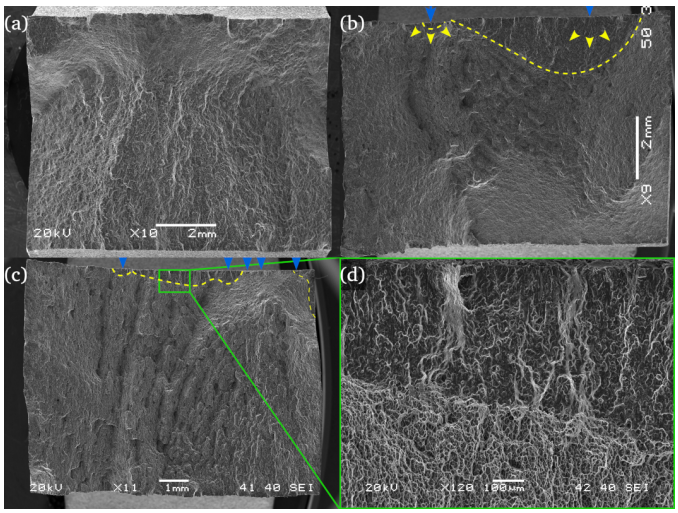

Fig. 13. Fractures of specimens loaded with $\varepsilon_a = 0.005$ mm/mm cut at: (a) 0°, (b) 45°, (c) 90°, with respect to the rolling direction; (d) magnified fragment of (c)

3.4. Fractography

Figures 12–14 present fracture surface images taken using a JEOL JSM-6480LV scanning electron microscope (SEM). The crack origins are marked with blue arrows, and the growth directions are marked with yellow arrows.

In the case of the low-strain amplitude $\varepsilon_a = 0.001$ mm/mm, for which the macro stress-strain response was purely elastic, a single origin was found on the fracture surface of the 0° specimen (Fig. 12a). The initiation zone smoothly transitions into the growth zone and then into the ductile zone with small, elongated dimples. For the 45° orientation, three origins were identified (Fig. 12b). The initiation zones are larger than those in the 0° direction and can be more clearly distinguished from the propagation zones. A change to ductile fracture with dimples is also more evident (Fig. 12d). For the 90° orientation, two origins can be seen (Fig. 12c). The crack growth zones are much larger than those in the other two directions, and the marks indicating the growth direction are affected by the texture orientation (compare Fig. 1 and Fig. 3c). The unstable crack growth zone can be distinguished by apparent dimples. At the

bottoms of the dimples, Al_2Cu intermetallic compounds were present (Fig. 12e) [36].

For the medium level of loading, ε_a = 0.005 mm/mm, the initiation zones are much smaller (Fig. 13a), and there are numerous cracks. Crack growth zones often comprise many initiated separately and then coalesced cracks (Fig. 13b–13d). In the 0° direction, the crack origins are extremely small and barely noticeable. With 45° and 90° orientations, a change to ductile fracture is even more evident than at the lower level of loading (Fig. 13d).

Figure 14 shows the fracture surfaces of specimens loaded with ε_a = 0.005 mm/mm. The origins of single cracks were found only (Fig. 14), and they were tiny. For the 0° direction, tire tracks were often visible [58–60], and for the 45° direction, the area next to the origin resembled the elongated ductile dimples.

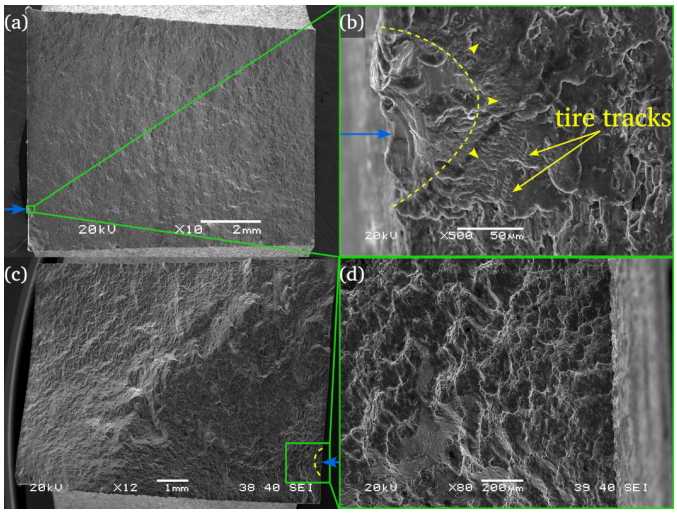

Fig. 14. Fractures of specimens loaded with ε_a = 0.010 mm/mm cut at: (a) and (b) 0°, (c) and (d) 45°, with respect to the rolling direction

Summing up, the fracture surfaces show typical differences between loading levels. At the low strain amplitudes, the crack origins are bigger, compared to higher ones. The crack growth zones are also bigger, as the loading was low enough to enable the crack growth. In contrast, the loading levels involving the elastic-plastic macro deformation resulted in exceedingly small origin and crack growth areas. At medium loading, the whole volume of material was strongly strained, and thus numerous cracks were initiated. When the highest level of loading was applied, it resulted in single origins, and the cracks grew quickly, leading to the failure of specimens (less than 200 cycles). Therefore, no other crack was initiated.

4. CONCLUSIONS

Based on the results of the strain-controlled, fully reversed fatigue tests of the AA2519 aluminium alloy, the following conclusions were drawn:

- The rolling process of the sheet resulted in a directional texture with strongly elongated grains in the rolling direction.
- Tensile tests revealed a minor impact of the structure directionality on monotonic properties. The differences in Young's modulus, yield stress, and ultimate tensile strength were less than 10%. Only the total elongation at the break of the specimen cut at 45° to the rolling direction was noticeably higher than for the other two.
- The cyclic stress-strain response was quite similar to the monotonic response. No significant cyclic hardening or softening was noted, and the cyclic yield stress was slightly lower than the monotonic one. For most of the specimens, the stress level remained remarkably stable during the tests.
- Fractographic analysis revealed that fracture morphologies vary depending on the rolling direction and level of deformation. The most pronounced differences were the size of the crack initiation zone and the distinctness of transition from the initiation zone to the growth zone.
- No important change in the fatigue life with a change in the specimen orientation regarding the rolling direction was observed. Assessing the results qualitatively, it can be concluded that one common ε-N curve can describe all the data points well. The differences between results for specimens cut in different directions seem not to be greater than the statistical dispersion within one group.

REFERENCES

[1] O.H. Duparc, "Alfred Wilm et les débuts du Duralumin," *Revue de Metallurgie. Cahiers D'Informations Techniques*, vol. 101, no. 5, pp. 353–360, 2004, doi: 10.1051/metal:2004157.

[2] A. Rutecka *et al.*, "Damage evolution in AA2124/SiC metal matrix composites under tension with consecutive unloadings," *Arch. Civ. Mech. Eng.*, vol. 20, no. 4, pp. 1–18, 2020, doi: 10.1007/s43452-020-00134-x.

[3] D. Boroński, I. Dzioba, M. Kotyk, A. Krampikowska, and R. Pala, "Investigation of the fracture process of explosively welded AA2519-AA1050-Ti6Al4V layered material," *Materials*, vol. 13, no. 10, p. 2226, May 2020, doi: 10.3390/ma13102226.

[4] T. Wang *et al.*, "Edge crack forming mechanism and the countermeasures in as-sintered 2024 aluminium alloy during cold rolling," *Fatigue Fract. Eng. Mater. Struct.*, vol. 43, no. 12, pp. 2812–2827, 2020, doi: 10.1111/ffe.13293.

[5] F.J. Mcmaster, C.P. Tabrett, and D.J. Smith, "Fatigue crack growth rates in Al-Li alloy, 2090. Influence of orientation, sheet thickness and specimen geometry," *Fatigue Fract. Eng. Mater. Struct.*, vol. 21, no. 2, pp. 139–150, 1998, doi: 10.1046/j.1460-2695.1998.00428.x.

[6] J.J. Fisher, L.S. Kramer, and J.R. Pickens, "Aluminum alloy 2519 in military vehicles," *Ad. Mater. Process.*, vol. 160, no. 9, pp. 43–46, 2002.

[7] L.S. Kramer, T.P. Blair, S.D. Blough, J.J. Fisher, and J.R. Pickens, "Stress-corrosion cracking susceptibility of various product forms of aluminum alloy 2519," *J. Mater. Eng. Perform.*, vol. 11, no. 6, pp. 645–650, 2002, doi: 10.1361/105994902770343647.

[8] X.P. Liang, H.Z. Li, L. Huang, T. Hong, B. Ma, and Y. Liu, "Microstructural evolution of 2519-T87 aluminum alloy obliquely impacted by projectile with velocity of 816 m/s," *Trans. Nonferr. Metals Soc. Chin. (Eng. Ed.)*, vol. 22, no. 6, pp. 1270–1279, 2012, doi: 10.1016/S1003-6326(11)61315-0.

[9] H. Gao, X.M. Zhang, H.Z. Li, and Y. Liu, "Microstructure Inhomogeneities in 2519A Aluminum Plate Penetrated by an Incendiary Projectile," *Mater. Sci. Forum*, vol. 546–549, pp. 1049–1054, 2007, doi: 10.4028/www.scientific.net/msf.546-549.1049.

[10] S.J. Pawel, "Scouting tests to examine potential corrosion of aluminum alloy 2519 during fabrication," Oak Ridge National Laboratory, United States, 1998. doi: 10.2172/304018.

[11] D.E. Hall, D.L. Mcdowell, and A. Saxena, "Crack tip parameters for creep-brittle crack growth," *Fatigue Fract. Eng. Mater. Struct.*, vol. 21, no. 4, pp. 387–401, 1998, doi: 10.1046/j.1460-2695.1998.00542.x.

[12] E.A. Starke and J.T. Staley, "Application of modern aluminum alloys to aircraft," *Prog. Aerosp. Sci.*, vol. 32, no. 2–3, pp. 131–172, 1996, doi: 10.1016/0376-0421(95)00004-6.

[13] S. Derda *et al.*, "Impact of the interface on the fatigue life of steel-based explosively welded heterostructured plates," *Arch. Civ. Mech. Eng.*, vol. 23, no. 3, p. 191, Aug. 2023, doi: 10.1007/s43452-023-00731-6.

[14] M. Kotyk, "Effect of cryogenic conditions on the critical crack tip opening displacement for the laminated material AA2519-AA1050-Ti6Al4V-T62," *J. Mater. Res. Technol.*, vol. 28, pp. 3319–3332, 2024, doi: 10.1016/j.jmrt.2023.12.211.

[15] M. Kotyk, "Analytic model of maximal experimental value of stress intensity factor Kq for AA2519–AA1050–Ti6Al4V layered material," *Materials*, vol. 13, no. 19, p. 4439, 2020, doi: 10.3390/ma13194439.

[16] D. Boroński, I. Dzioba, M. Kotyk, A. Krampikowska, and R. Pala, "Investigation of the fracture process of explosively welded AA2519-AA1050-Ti6Al4V layered material," *Materials*, vol. 13, no. 10, p. 2226, May 2020, doi: 10.3390/ma13102226.

[17] M. Kotyk, K. Kowalicki, and A. Skibicki, "Analysis of hardness of explosionally welded Al – Ti layer material and its base materials," *Postępy w Inżynierii Mechanicznej*, vol. 7, no. 13, pp. 25–37, 2019 (in Polish).

[18] B. Płonka, K. Żyłka, K. Remsak, M. Rajda, J. Zdunek, and D. Moszczyńska, "Influence of copper content on the structure and properties of aluminium alloys," *Arch. Civ. Mech. Eng.*, vol. 24, no. 1, pp. 1–11, Feb. 2024, doi: 10.1007/S43452-023-00811-7.

[19] A. Tzamtzis and A.T. Kermanidis, "Improvement of fatigue crack growth resistance by controlled overaging in 2024-T3 aluminium alloy," *Fatigue Fract. Eng. Mater. Struct.*, vol. 37, no. 7, pp. 751–763, 2014, doi: 10.1111/ffe.12163.

[20] A. Rutecka, Z.L. Kowalewski, K. Pietrzak, L. Dietrich, and W. Rehm, "Creep and low cycle fatigue investigations of light aluminium alloys for engine cylinder heads," *Strain*, vol. 47, pp. 374–381, Dec. 2011. doi: 10.1111/j.1475-1305.2010.00779.x.

[21] N. Dahdah *et al.*, "Damage Investigation in A319 Aluminium Alloy by X-ray Tomography and Digital Volume Correlation during In Situ High-Temperature Fatigue Tests," *Strain*, vol. 52, pp. 324–335, Aug. 2016, doi: 10.1111/str.12193.

[22] H. Li, Z. Li, M. Song, X. Liang, and F. Guo, "Hot deformation behavior and microstructural evolution of Ag-containing 2519 aluminum alloy," *Mater. Des.*, vol. 31, no. 4, pp. 2171–2176, 2010, doi: 10.1016/j.matdes.2009.10.061.

[23] H.Z. Li, X.M. Zhang, M.A. Chen, and Z.P. Zhou, "Effects of Ag on microstructure and mechanical properties of 2519 aluminum alloy," *J. Cent. South Univ. Technol.*, vol. 13, no. 2, pp. 130–134, 2006, doi: 10.1007/s11771-006-0143-0.

[24] I.J. Polmear, "3 - Wrought aluminium alloys," in *Light Alloys* (4th Ed.), I.J. Polmear, Ed., Oxford: Butterworth-Heinemann, 2005, pp. 97–204. doi: 10.1016/B978-075066371-7/50007-4.

[25] Z.-T. He, W.-H. Liu, Y.-Q. Chen, and C.-P. Tang, "Dynamic mechanical properties and microstructure evolution of 2519A aluminum alloy at low temperature," *Trans. Mater. Heat Treat.*, vol. 36, no. 4, pp. 62 – 67, 2015.

[26] L. Ye, G. Gu, X. Zhang, D. Sun, H. Jiang, and P. Zhang, "Dynamic properties evaluation of 2519A aluminum alloy processed by interrupted aging," *Mater. Sci. Eng. A*, vol. 590, pp. 97–100, 2014, doi: 10.1016/j.msea.2013.10.016.

[27] M. Kotyk and P. Strzelecki, "Determination of the Region of No Effect of the Notch on Fatigue Life of Aa2519 T62 Aluminium Alloy," *Adv. Sci. Technol. Res. J.*, vol. 18, no. 5, pp. 156–174, 2024, doi: 10.12913/22998624/190159.

[28] L. Ye, G. Gu, J. Liu, H. Jiang, and X. Zhang, "Influence of Ce addition on impact properties and microstructures of 2519A aluminum alloy," *Mater. Sci. Eng. A*, vol. 582, pp. 84–90, 2013, doi: 10.1016/j.msea.2013.06.028.

[29] Y. Li, L. Ye, X. Zhang, and D. Sun, "Effects of Cr and Yb additions on microstructures and mechanical properties of 2519A aluminum alloy," *J. Cent. South Univ.-Sci. Technol.*, vol. 45, no. 7, pp. 2182–2186, 2014.

[30] L. Liu, J.-H. Chen, S.-L. Xia, S.-S. Yang, and S.-B. Wang, "Effect of element V on microstructure and mechanical properties of 2519 alloy," *Trans. Mater. Heat Treat.*, vol. 35, no. 4, pp. 78–83, 2014.

[31] X.-M. Zhang *et al.*, "Effects of Yb addition on microstructures and mechanical properties of 2519A aluminum alloy plate," *Trans. Nonferr. Metals Soc. Chin.-Eng. Ed.*, vol. 20, no. 5, pp. 727–731, 2010, doi: 10.1016/S1003-6326(09)60205-3.

[32] W.T. Wang *et al.*, "Influences of Ce addition on the microstructures and mechanical properties of 2519A aluminum alloy plate," *J. Alloys Compd.*, vol. 491, no. 1–2, pp. 366–371, 2010, doi: 10.1016/j.jallcom.2009.10.185.

[33] M.J. Haynes and R.P. Gangloff, "Elevated temperature fracture toughness of AI-Cu-Mg-Ag sheet: Characterization and modeling," *Metall. Mater. Trans. A Phys. Metall. Mater. Sci.*, vol. 28, no. 9, pp. 1815–1829, 1997, doi: 10.1007/s11661-997-0112-8.

[34] M. Kotyk, D. Boroński, and P. Maćkowiak, "The influence of cryogenic conditions on the process of AA2519 aluminum alloy cracking," *Materials*, vol. 13, no. 7, p. 1555, 2020, doi: 10.3390/ma13071555.

[35] G.M. Owolabi *et al.*, "Fatigue Responses of Three AA 2000 Series Aluminum Alloys," *J. Mater. Sci. Chem. Eng.*, vol. 7, no. 3, pp. 32–48, 2019, doi: 10.4236/msce.2019.73003.

[36] R. Kosturek, L. Śniezek, J. Torzewski, and M. Wachowski, "Low cycle fatigue properties of sc-modified AA2519-T62 extrusion," *Materials*, vol. 13, no. 1, p. 220, 2020, doi: 10.3390/ma13010220.

[37] R. Kosturek, J. Torzewski, Z. Joska, M. Wachowski, and L. Śnieżek, "The influence of tool rotation speed on the low-cycle fatigue behavior of AA2519-T62 friction stir welded butt joints," *Eng. Fail. Anal.*, vol. 142, p. 6756, Jul. 2022, doi: 10.1016/j.engfailanal.2022.106756.

[38] H. Yan Miao, M. Lévesque, and F.P. Gosselin, "Eigenstrain-based analysis of why uniformly shot peened aluminium plates bend more in the rolling direction," *Strain*, vol. 59, no. 6, p. e12451, Dec. 2023, doi: 10.1111/STR.12451.

[39] P.A. Faucheux, H.Y. Miao, M. Lévesque, and F.P. Gosselin, "Peen forming and stress peen forming of rectangular 2024–T3 aluminium sheets: Curvatures, natural curvatures and residual stresses," *Strain*, vol. 58, no. 2, p. e12405, Apr. 2022, doi: 10.1111/STR.12405.

[40] M. Kalina, V. Schöne, B. Spak, F. Paysan, E. Breitbarth, and M. Kästner, "Fatigue crack growth in anisotropic aluminium sheets – phase-field modelling and experimental validation," *Int. J. Fatigue*, vol. 176, p. 107874, Nov. 2023, doi: 10.1016/J.IJFATIGUE.2023.107874.

[41] R. Kosturek *et al.*, "Study on Symmetry and Asymmetry Rolling of AA2519-T62 Alloy at Room-Temperature and Cryogenic Conditions," *Materials*, vol. 15, no. 21, p. 7712, 2022, doi: 10.3390/ma15217712.

[42] J. Han, M. Paidar, R.V. Vignesh, K.P. Mehta, A. Heidarzadeh, and O.O. Ojo, "Effect of shoulder features during friction spot extrusion welding of 2024-T3 to 6061-T6 aluminium alloys," *Arch. Civ. Mech. Eng.*, vol. 20, no. 3, p. 84, Sep. 2020, doi: 10.1007/s43452-020-00086-2.

[43] J. Klemenc, S. Glodež, M. Steinacher, and F. Zupanič, "LCF behaviour of high strength aluminium alloys AA 6110A and AA 6086," *Int. J. Fatigue*, vol. 177, p. 107971, Dec. 2023, doi: 10.1016/j.ijfatigue.2023.107971.

[44] R. Sepe, V. Giannella, N. Razavi, and F. Berto, "Characterization of static, fatigue and fracture behaviour of the aluminium-lithium alloy Al-Li 2198-T851," *Int. J. Fatigue*, vol. 166, p. 107265, Jan. 2023, doi: 10.1016/J.IJFATIGUE.2022.107265.

[45] A. Lipski, "Change of specimen temperature during the monotonic tensile test and correlation between the yield strength and thermoelasto-plastic limit stress on the example of aluminum alloys," *Materials*, vol. 14, no. 1, p. 13, Jan. 2021, doi: 10.3390/ma14010013.

[46] H. Hu and X. Wang, "Effect of heat treatment on the in-plane anisotropy of as-rolled 7050 aluminum alloy," *Metals (Basel)*, vol. 6, no. 4, p. 79, Apr. 2016, doi: 10.3390/met6040079.

[47] F. Ye *et al.*, "Influence of different rolling processes on microstructure and strength of the Al–Cu–Li alloy AA2195," *Prog. Nat. Sci.-Mater. Int.*, vol. 32, no. 1, pp. 87–95, Feb. 2022, doi: 10.1016/j.pnsc.2021.10.009.

[48] R. Shabadi, S. Suwas, S. Kumar, H.J. Roven, and E.S. Dwarkadasa, "Texture and formability studies on AA7020 Al alloy sheets," *Mater. Sci. Eng. A*, vol. 558, pp. 439–445, Dec. 2012, doi: 10.1016/j.msea.2012.08.024.

[49] Y. Chen *et al.*, "The fatigue crack growth behaviour of 2524-T3 aluminium alloy in an Al2O3 particle environment," *Fatigue Fract. Eng. Mater. Struct.*, vol. 43, no. 10, pp. 2376–2389, 2020, doi: 10.1111/ffe.13307.

[50] X.Y. Long *et al.*, "Effect of austempering temperature on microstructure and cyclic deformation behaviour of multiphase low-carbon steel," *Arch. Civ. Mech. Eng.*, vol. 23, no. 3, p. 201, Aug. 2023, doi: 10.1007/s43452-023-00735-2.

[51] W. Ramberg and W.R. Osgood, "Description of stress-strain curves by three parameters," Report NACA-TN-902,1943. [Online]. Available: http://hdl.handle.net/2060/19930081614

[52] R. Fincato, T. Yonezawa, and S. Tsutsumi, "Numerical modeling of cyclic softening/hardening behavior of carbon steels from low- to high-cycle fatigue regime," *Arch. Civ. Mech. Eng.*, vol. 23, no. 3, p. 164, Aug. 2023, doi: 10.1007/s43452-023-00698-4.

[53] J. Morrow, "Cyclic Plastic Strain Energy and Fatigue of Metals," in *Internal Friction, Damping, and Cyclic Plasticity*, B.J. Lazan, Ed., ASTM Special Technical Publication No. 378, 1965. doi: 10.1520/stp43764s.

[54] O.H. Basquin, "The exponential law of endurance tests," *Proc. Am. Soc. Test. Mater.*, vol. 10, pp. 625–630, 1910, https://www.scribd.com/document/465517629/Basquin-The-Exponential-Law-of-Endurance-Tests-pdf

[55] S.S. Manson, "Behavior of Materials Under Conditions of Thermal Stress," Report NACA-TR-1170 1954. doi: 10.1016/s0016-0032(38)90451-x.

[56] L.F. Coffin, "A study of the effects of cyclic thermal stress on a ductile metal," *Trans. Am. Soc. Mech. Eng.*, vol. 76, pp. 931–950, 1954.

[57] Z. Dong, X.F. Xie, J. Li, Y. Wan, and C. Wang, "Microstructure formation and fatigue performance of duplex stainless steel 2205 welded joints by electric resistance welding," *Arch. Civ. Mech. Eng.*, vol. 23, no. 3, p. 180, Aug. 2023, doi: 10.1007/s43452-023-00726-3.

[58] J. Zhang, X. Shi, and B. Fei, "High cycle fatigue and fracture mode analysis of 2A12–T4 aluminum alloy under out-of-phase axial–torsion constant amplitude loading," *Int. J. Fatigue*, vol. 38, pp. 144–154, May 2012, doi: 10.1016/j.ijfatigue.2011.12.017.

[59] Y. Chen, J. Zhou, C. Liu, and F. Wang, "Effect of pre-deformation on the pre-corrosion multiaxial fatigue behaviors of 2024-T4 aluminum alloy," *Int. J. Fatigue*, vol. 108, pp. 35–46, Mar. 2018, doi: 10.1016/j.ijfatigue.2017.11.008.

[60] Y. Chen, P. Xu, C. Liu, F. Wang, and H. Song, "Multiaxial fatigue behavior and life prediction of 7075-T651 aluminum alloy under two-step loading," *Eng. Fract. Mech.*, vol. 230, p. 107007, May 2020, doi: 10.1016/j.engfracmech.2020.107007.